Hydrogen fuel cell aircraft for the Nordic market

International Journal of Hydrogen Energy 61 (2024) 650–663

Contents lists available at ScienceDirect

International Journal of Hydrogen Energy

journal homepage: www.elsevier.com/locate/he

Hydrogen fuel cell aircraft for the Nordic market

Christian Svensson [a,*], Amir A.M. Oliveira [b], Tomas Grönstedt [a]

[a] Division of Fluid Dynamics, Department of Mechanics and Maritime Sciences, Chalmers University of Technology, Gothenburg, 412 96, Sweden
[b] Laboratory of Combustion and Thermal Systems Engineering, Department of Mechanical Engineering, Federal University of Santa Catarina, Florianópolis, 88040-900, Brazil

ARTICLE INFO

Keywords:
Hydrogen
Aircraft
Cryogenic
Boil-off
Multi-layer insulation
Proton-exchange membrane fuel cell

ABSTRACT

A model for a fuel cell propelled 50 PAX hydrogen aircraft is developed. In terms of year 2045 Nordic air travel demand this aircraft is expected to cover 97% of travel distances and 58% of daily passenger volume. Using an ATR 42 as a baseline, cryogenic tanks and fuel cell stacks are sized and propulsion system masses updated. Fuselage and wing resizing are required, which increases mass and wetted area. Sizing methods for the multi-stack fuel cell and the cryogenic tanks are implemented. The dynamic aircraft model is updated with models for hydrogen consumption and tank pressure control. For the Multi-layer insulation (MLI) tank a trade study is performed. A ventilation pressure of 1.76 bar and 15 MLI layers are found to be optimal for the design mission. A return-without-refuel mission is explored, where for a 10-hour ground hold 38.4% of the design range is retained out of the theoretically achievable 50%.

1. Introduction

The Swedish government put forward an initiative in 2018 to fully de-carbonize regional aviation by 2030, and a more ambitious goal of de-carbonizing all aviation departing within its borders by 2045 [1]. Sustainable Aviation Fuel (SAF) and technology improvements in current propulsion systems are proposed as short-term paths for achieving this. In the long run it is intended to replace kerosene combusting aircraft with fully electric and hydrogen powered aircraft. The 2030 and 2045 emission goals are to be met without harming economic growth and globalization.

Regional aircraft are estimated to have an 80% higher CO_2 intensity than narrow and wide bodied aircraft [2]. CO_2 intensity simply refers to the mass of CO_2 produced per passenger kilometer for a full aircraft. A large portion of this efficiency difference is believed to relate to the greater improvement efforts that have gone into narrow and wide body aircraft [2]. In addition, it is estimated that more than a third of global CO_2 emissions can be attributed to passenger flights under 2000 km [2]. It should therefore be possible to motivate a targeted effort on reducing the climate impact of aircraft optimized for flights under 2000 km [3]. The fact that shorter range aircraft also offer a better potential for being electrified, motivates the combined study of high efficiency aircraft targeting electrification. These aspects have together contributed to a number of recent aircraft development efforts in the area of electrification [4–7].

While regional hydrogen-powered aircraft might not offer the same range as its kerosene and SAF counterparts [8], the zero in-flight CO_2 emissions promises to be very valuable for reducing climate impact. For hydrogen powered aircraft two propulsion architectures compete, they may either be fuel cell propelled or be based on hydrogen combustion. The combustion-based concept is expected to be more compact and offer a better potential for longer ranges, as is indicated in Fig. 1. For shorter ranges fuel cell aircraft may alternatively be used, in particular since they promise to also remove the NO_x emissions [9]. The fuel cell aircraft will only exhaust water, and is therefore left with contrail formation as its sole mechanism for impacting the climate negatively. Although the fuel cell aircraft will have a higher frequency of contrail formation than its combustion counterparts, it is believed that they are less persistent and hence the impact on the climate is expected to be less [10]. Furthermore, the cruise altitude for regional aircraft is frequently lower than the Appleman–Schmidt limit for contrail formation [11].

Several studies have investigated the potential performance of hydrogen aircraft [13–20], but these studies have been limited to medium and long-range flights as these missions have the greatest potential to reduce climate impact. Studies on aircraft with seating capacities of 19 to 50 PAX and ranges between 800 to 1200 km are less common. Burschyk et al. have studied design trades for hydrogen stored in external wing pods [21]. Zaghari et al. [22] studied the use of multi-stack fuel cell configurations for regional aircraft. Zaghari's work gives support for conceptual fuel cell designs in the megawatt class required for regional aircraft. Gao et al. investigated a commuter and a regional aircraft both powered by fuel cells, where the energy

* Corresponding author.
E-mail address: chrissv@chalmers.se (C. Svensson).

https://doi.org/10.1016/j.ijhydene.2024.02.382
Received 4 December 2023; Received in revised form 26 February 2024; Accepted 29 February 2024
Available online 4 March 2024

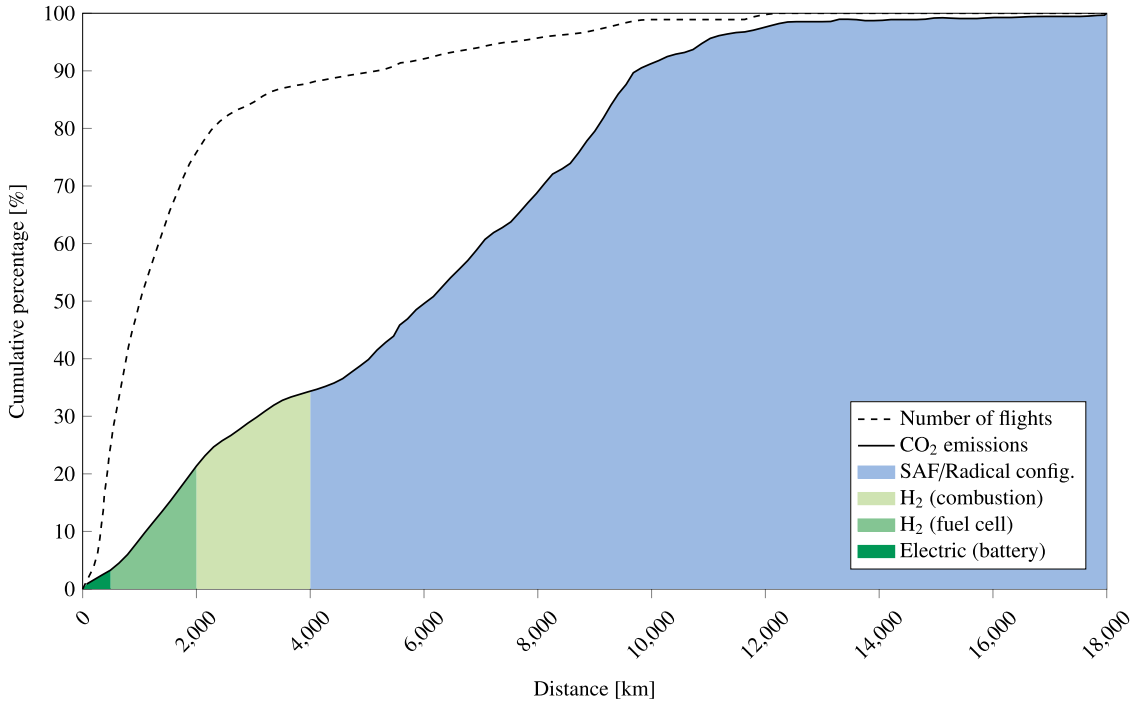

Fig. 1. Number of departing commercial flights and CO_2 emissions as a function of flight distance emanating from Schiphol airport during 2018. Colored segments represent proposed future share of propulsion types.
Source: Reproduced from [12].

demand was decreased by 8% and 10% respectively compared to their kerosene counterparts [23]. Verstraete et al. studied liquid hydrogen tank designs for a regional aircraft, where the choice of insulation type had a large impact on fuselage size [24]. Mukhopadhaya analyzed the performance of an ATR 72 turboprop aircraft retrofitted with a fuel cell propulsion system. In the study the hydrogen storage was installed in the existing fuselage by removing seating capacity [25]. A reduced energy need was noted, but at the cost of payload capacity and range. Seeckt et al. studied two hydrogen fueled freighter aircraft in a regional turboprop configuration [26], one where the tank was integral to the fuselage and used the full cross-sectional area, and one non-integral design where the fuselage required stretching. The empty weight increased by 2% and 7% respectively, while the take-off weight decreased by 5% and 3%. Both versions consumed 10% less energy than their kerosene counterpart.

As was shown in [23,25], fuel cell aircraft for shorter ranges consume less energy than their kerosene counterparts, despite increased aircraft empty weight. This is due to the high efficiencies achieved by modern proton-exchange membrane fuel cells (PEMFC). With current PEMFC technology another concern is also the large amount of heat that needs to be rejected via the relatively small temperature difference to the ambient. Current PEMFCs operate at very low temperatures of around 60–80 °C and therefore require large heat exchangers, which add weight and drag to the aircraft. High temperature PEMFCs which promise to operate at 120 °C or above [27], would perform much better in this respect.

Hybridized propulsion systems consisting of a fuel cell system and an electrical motor coupled to a turboprop are also interesting options for this class of aircraft. Fuel cell systems are less power-dense compared to conventional turboprops, and suffer from cooling challenges as previously mentioned. A hybrid strategy could therefore save weight and make the aircraft more efficient, by not having to solely rely on the fuel cell power at take-off. Palladino et al. [28] studied a regional aircraft using hydrogen-based hybrid propulsion. The study targeted a 70–80 PAX aircraft and a 23% reduction in CO_2 was noted for an optimal 45% degree of hybridization. Rischmüller et al. studied a regional aircraft retrofitted with a fuel cell system to hybridize the sustainable aviation fuel (SAF) combustion propulsion [29]. By allocating 20% of the required propulsive power to the fuel cell system, a 12.9% reduction of SAF fuel consumption was seen. The retrofit resulted in an 18.1% reduction of payload capacity.

In the light of the review of the current literature we note that there is lack of studies on short range aircraft propelled by a pure fuel cell drive train. The study closest to this work is probably the retrofit study by Mukhopadhaya [25]. Herein, we instead study a stretch of the baseline aircraft fuselage and a re-sizing of the wing as a function of the tank and fuel cell drive train sizing. Additionally, the available literature does not consider regional variations such as population density, climate and airport infrastructure, which are important for an aircraft concept's commercial feasibility. Fig. 2 shows how the larger population centers of Sweden, Finland and Norway are situated on the southern halves. In the case of Norway, the country is split by a large mountain range, causing people to be spread out along the coast and in many cases preventing efficient travel by road or rail. This study will size a future hydrogen fuel cell electric aircraft tailored to cover a large portion of Nordic air travel demand. Design parameters related to the hydrogen storage such as ventilation pressure and insulation thickness will be varied in order to investigate the impact on fuel burn and help select a suitable aircraft design for the Nordic market. To support its introduction into an airport network where hydrogen infrastructure may only be partially available, the feasibility of return-trip missions without refueling is investigated. With a substantial *return-without-refuel range*, such an aircraft could enable operation at a much earlier stage.

2. Mission modeling

2.1. Nordic air travel demand and the design range

In a recent study performed by Amadori et al. [31], a model is developed to predict the future air travel demand within Sweden, Norway and Finland. The model is a "gravity model" which attempts to predict the frequency of travel between two given cities. The predictions are based on parameters such as population and GDP growth,

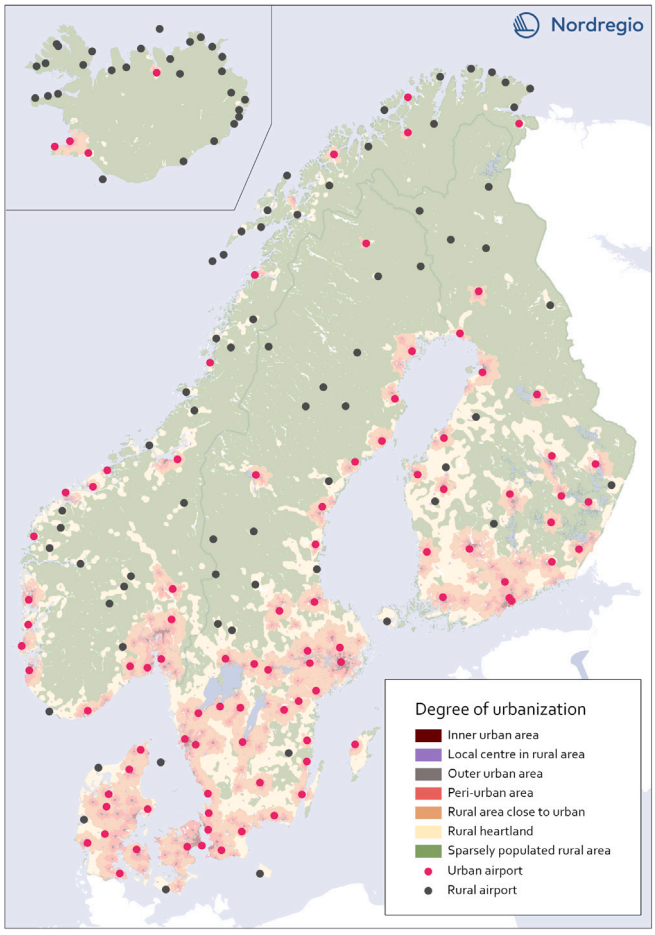

Fig. 2. Map of Nordic airports by degree of urbanization [30].

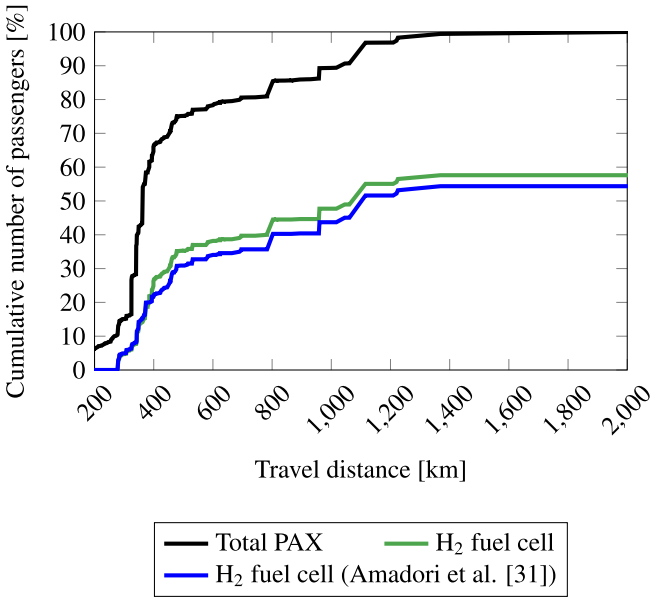

Fig. 3. Projected future air travel demand in the Nordics, adapted from [31]. The gap to the Total PAX curve is comprised of SAF, H_2 combustion & battery electric flights.

and whether a city has major institutions such as universities or large hospitals [31]. In the Swedish case, a model for predicting regional air travel in the year 2045 is available from Trafikverket (Swedish Transport Administration). This model is used for tuning the coefficients that weigh each gravity parameter. A model of similar detail was not available for Norway and Finland and therefore the Swedish gravity weighting coefficients were used together with Norwegian and Finnish GDP growth estimates. A growth prediction was then applied to the passenger volume of each route. The demand model produces daily passenger volumes between two given cities, A and B, where the total volume is split evenly between the routes A-to-B and B-to-A.

In order to include the effect of inter-country travel on the travel demand, data from Swedavia [32] of quarterly passenger volumes between Swedish airports and the Nordic capitals has been added to the original demand model presented in [31]. The data is collected at different Swedish airports and consists of both departing to and arriving from Oslo and Helsinki during year 2019. The Swedavia data was averaged across the quarters, split into daily passenger volumes and distributed evenly over routes A-to-B and B-to-A. The major change from the original data [31] is that the volume of medium range flights has increased.

As seen from Fig. 3, the Nordic demand model suggests that if a maximum range of 1200 km is set for the hydrogen fuel cell aircraft, a very large portion of the projected Nordic market need could be covered. Designing the aircraft for this range would remove the need for H_2 combustion or SAF aircraft for Sweden and Finland. For the Norwegian market a 1200 km range aircraft could serve 97% of the total air travel demand, and could have to be complemented by SAF or hydrogen combustion aircraft only for the remaining 3%. In total, the Nordic market could potentially be covered to 99.2% by a hydrogen fuel cell aircraft having a 1200 km range. We would like to emphasize that a commercial manufacturer of a future fuel cell aircraft would select the aircraft range based on a mixture of anticipated global markets, rather than to focus solely on the Nordic market. Hence, the conceptual aircraft design studies carried out in this paper, should be understood as an assessment of the performance of an aircraft ideal for the Nordic market rather than a prediction of the best range of future fuel cell aircraft.

Clearly, some routes are more suitable for operation by larger than 50 PAX aircraft, and applying our updated demand model we estimate that hydrogen fuel cell aircraft would be suitable for use in 58% of the cumulative number of passengers. We also note a slight increase in demand for the fuel cell aircraft (green curve) as compared to the Amadori et al. [31] model (blue curve) due to the inter-nordic operations not present in the original model. Notice that the difference between the total number of passengers curve (black) and the fuel cell aircraft use, is comprised of primarily SAF but to some extent also hydrogen combusting aircraft [31]. The initial 10.1% of the passenger transport is carried out solely by battery electric aircraft.

2.2. Mission analysis

Two mission types are considered:

1. The design mission (1200 km range) as introduced in the previous section.
2. A return-without-refuel mission, that is flying from A-to-B, then B-to-A without refueling.

Both missions are illustrated in Fig. 4. The return-without-refuel mission is studied to better understand the compromises incurred for early Nordic market operation, for which only a limited number of airports may have received a hydrogen infrastructure.

The design mission consists of a climb, cruise and descent segment to a destination airport. The horizontal distance of these segments constitutes the design range. Reserve fuel is accounted for by simulating a 20 min loiter at the destination airport, together with a diversion of 100 NM to an alternate airport, where a 30 min loiter is performed to

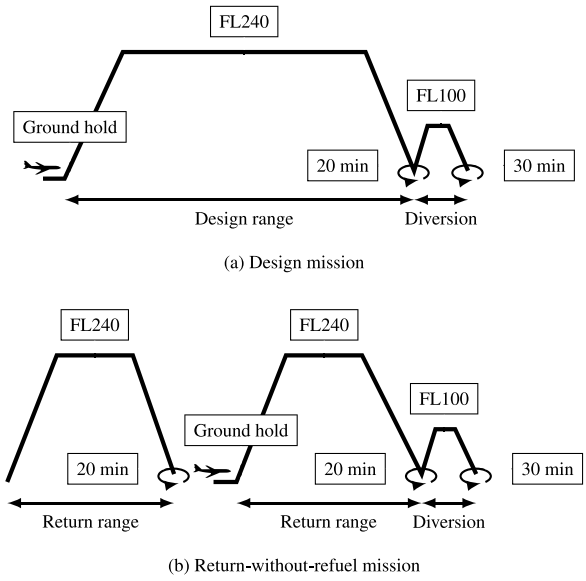

Fig. 4. The two different mission profiles used in the simulations.

Table 1
Missions studied.

Study	Mission type	Ground hold
Optimize tank design for minimal total fuel consumption	Design	No
Investigate effect of boil-off on design range	Design	0–12 h
Investigate effect of boil-off on return-without-refuel range	Return-without-refuel	0–12 h

account for final reserves. The return-without-refuel mission profile is similar to that of the design mission, but differs in the reserves. On the way to the destination airport, a successful attempt to land is performed directly after loitering for 20 min. The aircraft is then held on the ground for a specified duration, causing fuel to boil-off and potentially to be ventilated. On the way back to the origin airport, full reserves are assumed, that is the return is assumed to require a diversion mission as illustrated in Fig. 4(b).

The design mission is studied in two variants, both with and without ground hold. Thus, as specified in Table 1, three studies are carried in total.

3. Hydrogen aircraft technology

3.1. Hydrogen aircraft

The use of hydrogen in aircraft has been studied since WW2 and is today a well-researched area. Design studies conducted on airframes, hydrogen storage and engine technology have come a long way and concepts ranging from short-haul to long-haul have been proposed. During the oil crisis in the 1970's, NASA's Langley Research Center commissioned Lockheed-Martin to perform studies on liquid hydrogen subsonic passenger transport aircraft with a 1985 technology freeze date and an entry-into-service of 1990 [33,34]. A 1500 NM, 130 PAX short-range aircraft and a 5500 NM, 400 PAX long-range model both with a cruise speed of Mach 0.85 were proposed. The cryogenic tanks were integral to the fuselage and located forward and aft of the passenger compartment. Note that a forward tank would require an asymmetric shape to accommodate an access path from the cabin to the cockpit, which increases structural weight [35]. The tanks were constructed from aluminum and featured a closed-cell plastic foam insulating layer which was optimized for minimal boil-off. The short-range aircraft showed an 11% decrease in gross weight and a 3% increase in empty weight. Wing area and span width reduced with 2% and 6% respectively. However there was an 18% decrease in cruise lift-over-drag which was noted due to the increased fuselage wetted area. In the late 1980's Tupolev flew the Tu-155, a modified Tu-154 transport aircraft testing the use of hydrogen [36]. The cryogenic fuel was stored in an aft-mounted 15 m^3 tank. The results of the Tupolev project were carried over into the German–Russian Cryoplane project in the late 1990's, were LH_2 aircraft design as well as safety aspects were studied [37].

In the early 2000's the European Commission launched an extensive study of LH_2 aircraft in a project, also named Cryoplane [38,39]. Both conventional designs with "minimum change" of existing aircraft, and unconventional designs were proposed. The conventional fleet design proposal consisted of regional, medium and long-haul aircraft. The "small regional and business aircraft" had tanks fitted behind the rear pressure bulkhead and a wider than usual fuselage, to prevent excessive center-of-gravity shift during flight. Compared to its kerosene counterpart, a 14% increase in energy consumption was predicted. The "regional up to 100 seats" configuration had an aft tank as well as tanks fitted on top of the cabin. The increase in energy consumption was 14% for the turboprop configuration and 18% for the turbofan version. The "short and medium range aircraft" had similar tank configurations to the previously mentioned aircraft, and the "long range and very long range aircraft" instead had large forward and aft tanks, but no top-mounted tanks. Like the Lockheed studies, Cryoplane was able to prove technological viability, but deemed the costs of LH_2 production, storage and distribution to be the main hindrance [39].

More recently Boeing proposed its Phantom Eye, a long endurance UAV, featuring a liquid hydrogen tank and a piston-driven propulsion system [40]. In 2012 the aircraft operated for four consecutive days on an altitude of 65,000 ft [41]. ZeroAvia is a company focusing on hydrogen fuel cell-driven electric aircraft. They intend to demonstrate a 19 PAX aircraft with a 300 NM range by 2025 [5]. The company's first hydrogen-fuel cell powered flight occurred during 2020 in a converted Piper Malibu, which lasted for eight minutes. Universal Hydrogen recently made a successful flight of a Dash 8–300 retrofitted with a hydrogen fuel cell powertrain [42]. The company is currently developing a conversion kit for the beforementioned Dash 8, as well as the ATR 72. The liquid hydrogen tanks are encapsulated in air freight-like containers, which are then loaded into the aircraft's rear cargo door by ground crew. The idea is to fill these tanks at some central location, and then transport them to the airports like any other cargo.

3.2. Hydrogen storage

While hydrogen gas offers roughly a three times larger lower heating value (LHV) compared to regular jet fuel (kerosene), the density at atmospheric conditions is almost 9000 times lower [43,44]. This low density would result in infeasible storage volumes for most vehicles. Hence, the hydrogen gas (GH_2) is either stored in a compressed state (usually 350–700 bar) or in a cryogenic liquid state (LH_2). Compressed GH_2 at 700 bar has a density of 39.1 kg/m^3 [45]. The gaseous state is easier to maintain for longer duration not being sensitive to external heat transfer. On the other hand, the very high pressures require tanks with high structural capability which tend to make the designs quite heavy, often with hydrogen content below 5% of the total tank mass [46].

LH_2 has a boiling point of around 20 K at atmospheric pressure and has a density of 71.9 kg/m^3 [43]. The relatively high energy density of LH_2 makes it a feasible option for aircraft as compared to compressed GH_2, as the required mass for fuel and tank storage must be kept to a minimum. The LH_2 is stored at pressures slightly above atmospheric, typically a few bars, and therefore the tank's main concern is the cryogenic temperature. Pressure is still carefully controlled since any

external heat input to the liquid will cause it to boil and build up tank pressure. To minimize the fuel loss while keeping the structural weight low, LH_2 tanks require insulation with extremely low thermal conductivity, as well as a tank internal wall with a very low hydrogen permeability. The cryogenic condition also calls for tank wall materials of excellent strength, fracture and stiffness properties, while providing low weight. Suitable steels and aluminum alloys excel in all of the above criteria except weight. Composite materials such as carbon-fiber-reinforced-polymers (CFRP) have very high specific stiffness and strength properties, and can therefore be made into tanks of low mass. It is on the other hand more prone to hydrogen permeation, which subsequently causes composite tanks to require an inner liner made out of metal. This again increases the tank mass, and can cause structural issues caused by mismatched thermal expansion properties [47]. Development of liner-less CFRP technology is underway, but require further studies to become serviceable for LH_2 storage [48].

The state-of-the-art within cryogenic tank insulation is Multi-layer insulation (MLI), which is constructed by alternating thin radiation shields in the form of reflective materials such as Mylar to prevent radiative heat transfer, separated with a thin insulating material to prevent conduction between the layers. This technology has primarily seen use in space applications, as the only heat transfer mechanism in a vacuum is thermal radiation. For use in non-vacuum environments, a high-vacuum layer has to be incorporated to prevent thermal conduction through the space in between the reflective shields. MLI (in high-vacuum) can offer thermal conductivities in the range of 10^{-5}–10^{-8} W/m K [47,49], but require a vacuum-jacket strong enough to prevent buckling and ultimately a catastrophic loss of insulation against heat conduction. The performance of the MLI system can be enhanced by varying the layer density so that the layer density is lower at the cold boundary (by increasing the spacer material thickness), as it has been shown that conduction is the dominant mean of heat transfer there [50]. Another emerging technology is to enhance the MLI by pumping cryogenic GH_2 through a layer inside the MLI in order to further reduce the heat transfer from the ambient [50,51]. Foam-type materials are interesting due to their low cost and relative low densities. It is also more feasible to implement due to its wide use presently. Thermal conductivities are orders of magnitude larger than MLI, and require a vapor barrier to prevent moisture absorption which would increase the conductivity to catastrophic levels. Polyurethane foam has a thermal conductivity ranging from 10^{-2}–10^{-4} W/m K and a density of 32–64 kg/m^3.

The LH_2 tanks modeled herein assume an MLI insulation system with constant layer density because of its excellent thermal properties and low weight penalty. In ground operations MLI has also been shown to outperform all variations of foam-type insulation [21]. It is also a flexible system in terms of the ability to vary the amount of layers and layer density without having to change the material. The tank design is selected as a compromise between tank mass and heat transfer performance, and a trade study is performed as part of this analysis.

4. Aircraft modeling

4.1. Sizing routines

The parameterized **aircraft model** is integrated in the SUAVE open source tool [52]. A baseline ATR 42 aircraft is initially modeled. The baseline aircraft's weight is split into individual weights for the fuselage, wing and propulsive system using SUAVE's weight correlation methods [52]. The optimizer then sets fuel volume, tank ventilation pressure and insulation thickness. Given these parameters, the LH_2 tank is sized, which dictates the fuselage length. As part of the design process, resizing of the wing, propulsive system and fuselage is accounted for. It is thereafter possible to update the baseline aircraft weight breakdown. With an updated weight estimate for the aircraft, the fuel cell system and wing area are sized to maintain the baseline aircraft's wing loading and power-to-weight ratio, respectively.

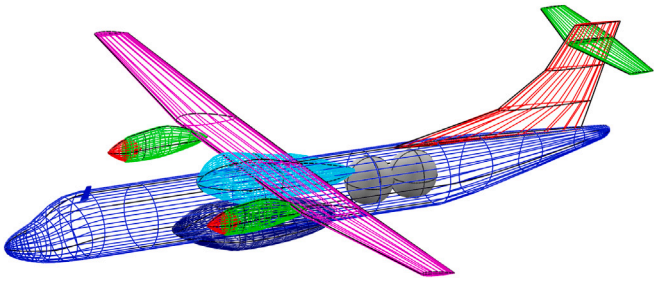

Fig. 5. Aircraft rendering illustrating tank installation.

The **tank design** routine will initially attempt to create a spherical tank due to its superior mechanical and thermodynamic properties. The outermost radius of the tank is constrained by the condition $r_4 \leq 0.92 \cdot r_{fuselage}$. Hence, it is assumed that 8% of the fuselage radius is occupied by internal structure. If the spherical tank ends up exceeding the maximum allowable radius, a cylindrical section is added to the tank between the two spherical end-caps. With the overall length of the tank known, the required extension of the fuselage is added. This translates the aft up-swept tail section as well as the empennage assembly rearward. The original cabin layout is therefore unchanged. Fig. 5 illustrates the location of the tanks, in this case two spherical.

SUAVE's built-in capabilities have been extended with two new methods for modeling hydrogen fuel cell aircraft with cryogenic storage. Firstly, a routine for mechanically sizing the tank and its insulation properties is implemented in order to calculate the tank size and mass. Secondly, a method for calculating the pressure inside the tank and its required ventilation mass flow is implemented in the mission solving routine. It is assumed that the total required fuel volume is split over two identical tanks, and that fuel is withdrawn and ventilated equally for both tanks. Details on the tank modeling is contained are Appendix A listing the equations used.

The **drive train** is comprised of a fuel cell stack and auxiliary components. The fuel cell stacks are comprised of single cell units connected in series to develop an appropriate voltage. To develop the suitable power, multiple stacks are then configured in parallel into a so-called series–parallel multi-stack configuration. Such a configuration will allow for some individual stack control and at the same time provide redundancy against stack failure [53]. Proton-exchange membrane fuel cells (PEMFC) are considered and a polarization function is used taking activation, ohmic and concentration losses into account [54] with model coefficients provided by Datta [55]. The complete model is found in Appendix B and resulting stack level design data are given in the next section. For the auxiliary components the largest power consumers are modeled, that is the power requirement for compressing the air and for powering the circulation pumps for the cooling system. These auxiliary components are referred to as Balance-of-Plant (BoP) devices. The air compressor is designed to boost the ram intake pressure to a stack pressure of 2.5 atm and has its worst-case operating point occur during cruise flight. The cooling system is designed to cope with the worst-case take-off scenario, an ambient temperature of 40 °C. The BoP power consumption varies over the mission as the freestream temperature and pressure as well as power demand changes with the flight conditions. With the stack and BoP sized, it is possible to form an energy network with SUAVE's existing propeller and electric motor methods.

4.2. Mission performance of the tank system

To illustrate how the tank model and its pressure control is managed its dynamic behavior throughout the aircraft design mission, is plotted

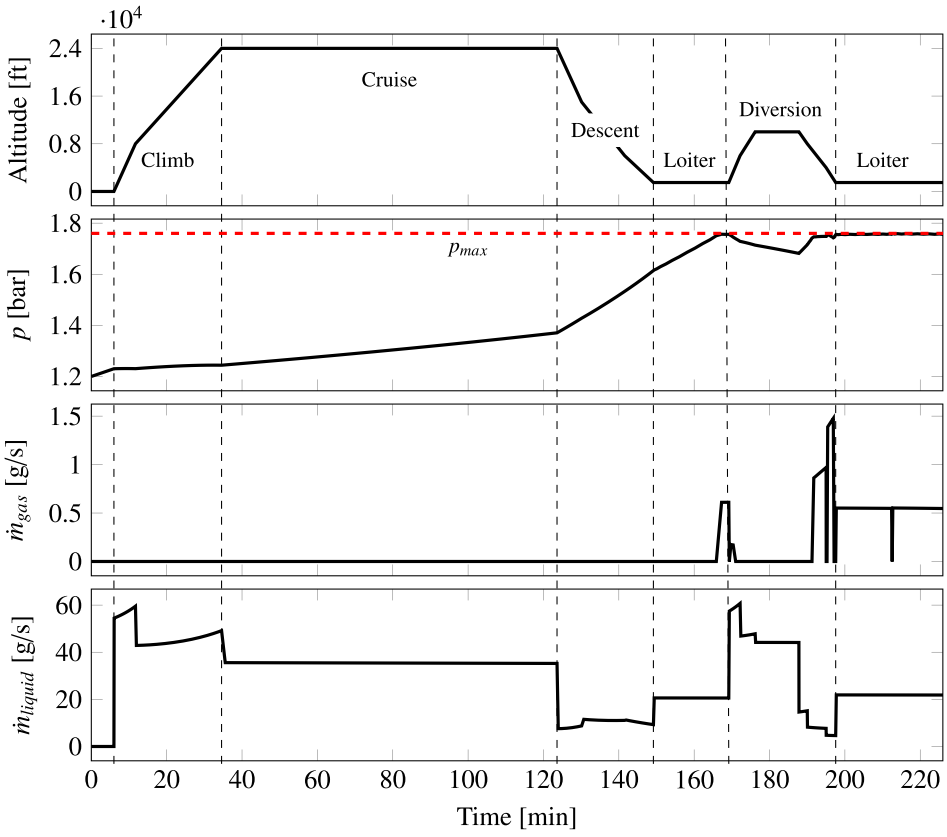

Fig. 6. Variation of altitude, tank pressure, ventilation mass rate and fuel mass rate during the design mission (p_{max} = 1.76 bar, N_{MLI} = 10).

in Fig. 6. Altitude variation, tank pressure, ventilation rate and fuel flow is plotted over mission time. Heat transfer to the tank is computed throughout the mission but it is only in the diversion part of the design mission that fuel venting is necessary to keep the tank pressure below the maximum allowed tank pressure p_{max}.

At each solver iteration, the computed tank pressure time-series vector is checked not to exceed a threshold value p_{max}, that is the ventilation pressure. Over-pressure in the tank is corrected for by calculating the venting mass flow $\dot{m}_{gas}$. It is obtained from Eq. (A.6), by solving for a required change in the pressure derivative necessary to go from the current tank state to a target state at which the tank pressure is at the threshold. The tank pressure is dependent on which mission segment is being executed as well as remaining fuel levels. For instance, a climb mission segment has a large fuel flow due to the high power draw. Liquid hydrogen may then be withdrawn from the tank at such a high rate that the pressure may decrease to a minimum value. On the contrary the descent, cruise and loiter use less power and can therefore cause the pressure to increase until the ventilation pressure is reached.

4.3. The SUAVE software

The conceptual aircraft design software Stanford University Aerospace Vehicle Environment (SUAVE) [56], is used throughout this paper. The open-source code is written in Python and is fully available and documented at GitHub [57]. The software is comprehensive in the way that it allows a user to design, simulate and optimize both conventional and unconventional aircraft types with various propulsion systems [52]. For simulating missions it is fully physics based and develops the aerodynamic performance of the aircraft around a built-in low-fidelity CFD solver [52]. Classical empirical methods such as weight estimations are also implemented. SUAVE is built for computational efficiency and uses pseudo spectral methods for solving differential equations such as the flight mechanics during a mission simulation [52]. The code is also robust in optimization and will always produce smooth output, which allows for rapid and full exploration of the design space [52].

Table 2
Top-level design requirements for the aircraft.

Parameter	Requirement
Cert. type	CS-25
Crew	2 pilots, 1 flight attendant
Passenger capacity	50 (110 kg total per passenger)
Design range	648 NM
Reserves	20 min loiter (200 kts, 1500 ft) 100 NM alternate
Final reserve	30 min loiter (200 kts, 1500 ft)
Cruise performance	300 kts @ FL240
Propulsion type	Electrical propeller, PEMFC, LH_2 fuel system

5. Results and discussion

5.1. Design specifications

From the details of the passenger demand model it was chosen to size and simulate a propeller-electric short-range aircraft driven by PEMFCs and LH_2. The passenger capacity is set to 50 PAX, proposed as one of the suitable aircraft configurations for the Nordic market [31]. The design range was set to 648 NM (1200 km) as to cover a large portion of the demand in the Nordics. Table 2 lists the top-level requirements for the aircraft.

5.2. Parameter study: insulation and ventilation pressure

A parameter study was conducted to select the tank design condition:

- Ventilation pressure p_{max} was varied between 1.4 and 4.0 bar
- The number of insulation layers N_{MLI} were varied between 2 and 60

The change from 2 to 60 N_{MLI} corresponded to a thickness variation of 1 mm to 30 mm. To guarantee the mechanical integrity of the tank, the pressure should never be allowed to go below ambient pressure. We therefore impose a minimum pressure constraint of $p_{min} = 1.2$ bar at any point in the mission consistent with Allidieris et al. [58].

The tank trade study results in the design space as shown in Fig. 7(a), where the mission fuel consumption of hydrogen is displayed. The dashed lines indicate the tank design's gravimetric index (GI). The tank mass variation is dominated by the inner and outer aluminum walls. It is primarily the inner wall that increases as p_{max} is increasing. This is the predominant effect on the gravimetric index. It is only increasing slowly with N_{MLI}. The insulation mass is only in the order of 1% of the aluminum mass. It should be noted however, that the increase in the outer diameter due to the fitting of the insulation also contributes to increasing the mass of the outer tank wall indirectly as seen from Eq. (A.5).

For lower values of N_{MLI} the total fuel consumption begins to increase due to boil-off and an increased need for venting during the mission. This is further aggravated when combined with low values of p_{max} resulting in additional venting due to that the p_{max} is reached earlier in the mission. For around $N_{MLI} \geq 8$ very little effect is seen on the mission fuel use. For these missions the insulation is so effective that the heat transfer is so low that the pressure rise during the mission will be slow enough to avoid the need for venting. There is slow increase in mission fuel burn due to the increased tank volume and mass slightly increasing both the aircraft mass and its drag. These effects actually combine to produce a minimum fuel burn as indicated by the white star in Fig. 7(a). This occurs at $p_{max} = 1.76$ bar and $N_{MLI} = 15$. At that point the gravimetric index is 0.555. For higher than $N_{MLI} = 16$ the insulation is so effective that the minimum pressure of $p_{min} = 1.2$ bar is reached early in a climb segment. This could easily be adjusted for either by fitting the tank with a heater or by simply letting the aircraft wait before take-off or filling the tank at a higher pressure. Further data on the optimal tank design can be found in Table 5.

By excluding the vented hydrogen and only plotting the fuel used by the fuel cell, it is seen that the variation in hydrogen use is quite small as is shown in Fig. 7(b). The aircraft maximum take-off mass is estimated at approximately 21 tonnes and the tank weight including the fuel is around 850 kg which corresponds to about 4% of the take-off mass. Modest variations in tank weight will therefore only have a minor impact on fuel burn. This insensitivity to tank gravimetric index is consistent with the Breguet range-analysis carried out by Adler et al. [59], where hydrogen regional aircraft with GI exceeding 45% suffered virtually no range penalty compared to its kerosene counterpart. The large differences in fuel burn between designs seen in Fig. 7(a) is primarily driven by the amount of hydrogen ventilated (and lost) due to boil-off, as seen in Fig. 7(c).

5.3. Resulting aircraft design

With an optimal tank established for the design mission, the resulting aircraft specifications can be presented. Both wing-loading and power-to-weight ratio have been kept fixed to not change the airport compatibility. The weight has significantly increased due to the fuselage extension to accommodate the tanks, as well as the weight of the fuel cell stacks. Table 3 compares the reference aircraft (ATR 42-600) with the new design.

Table 3
Comparison of weight, wing and fuselage specifications between the reference aircraft and new design. Parameters marked with (*) are considered estimates for the ATR 42.

	ATR 42-600	LH_2 PEMFC
MTOW	18600 kg	21049 kg
MZFW	17000 kg	20573 kg
Wing loading	341 kg/m^2	341 kg/m^2
Power-to-weight	0.192 kW/kg	0.192 kW/kg
Fuselage length	22.7 m	26.5 m
Fuselage fineness ratio	7.68	8.98
Fuselage wetted area*	208.2 m^2	243.6 m^2
Wing reference area	54.5 m^2	61.7 m^2
Wing aspect ratio*	10.9	10.9
Wing span	24.57 m	25.93 m
Wing taper ratio*	0.56	0.56
Flap configuration	Single-slotted	Single-slotted

Table 4
Specifications of the electric propulsion system (power figures will slightly vary depending on resulting aircraft mass). Per motor nacelle. Specific power is using net power.

Parameter	Specification
Fuel cell technology	PEMFC
Gross power	2093 kW
Net power	1840 kW
Total mass	1223 kg
BoP mass	531 kg
Specific power (incl. BoP)	1.50 kW/kg
Specific power (excl. BoP)	2.66 kW/kg
Stack pressure	2.5 atm
Stacks in parallel	3
Cells in series (per stack)	875
Total number of cells	2625
Cell area	996 cm^2
Cooling system type	Liquid-to-air radiator
Air system type	Ram intake withcompressor
Motor power density	7.9 kW/kg

The propulsion system consists of propellers driven by high-performance electrical motors using a fuel cell stack. Each wing has one propeller, one motor and one fuel cell stack. The specifications of the electrical propulsion is listed in Table 4. The resulting specific power of the stack design closely matches that of the US Department of Transport's 2025 technical targets for transportation fuel cell stacks [60]. The specific power for the electrical motor is based on the Honeywell design covered in [61]. Finally, the specifications for the optimal tank can be found in Table 5.

5.4. Effect of ground-hold time on range

After having decided on optimal tank design parameters for the design mission we now return to the two remaining studies as indicated in Table 1. In this section we then study the effect of ground hold on the design mission, and in the next section we study a return-without-refuel mission.

Using the optimal tank design, a ground hold time was added to the design mission before the first climb segment and was varied between 1 and 12 h. In essence a ground hold will cause boil-off to occur in the tank before flight, and as a result raise the initial tank pressure. If enough gas is ventilated on the ground before the flight, a significant decrease in range may be the consequence. As seen below in Fig. 8, range is not affected up to the two hour mark. The reduction in design range is observed to follow a linear trend as the ground hold time is increased. From zero to the two hour mark, the pressure rise due to

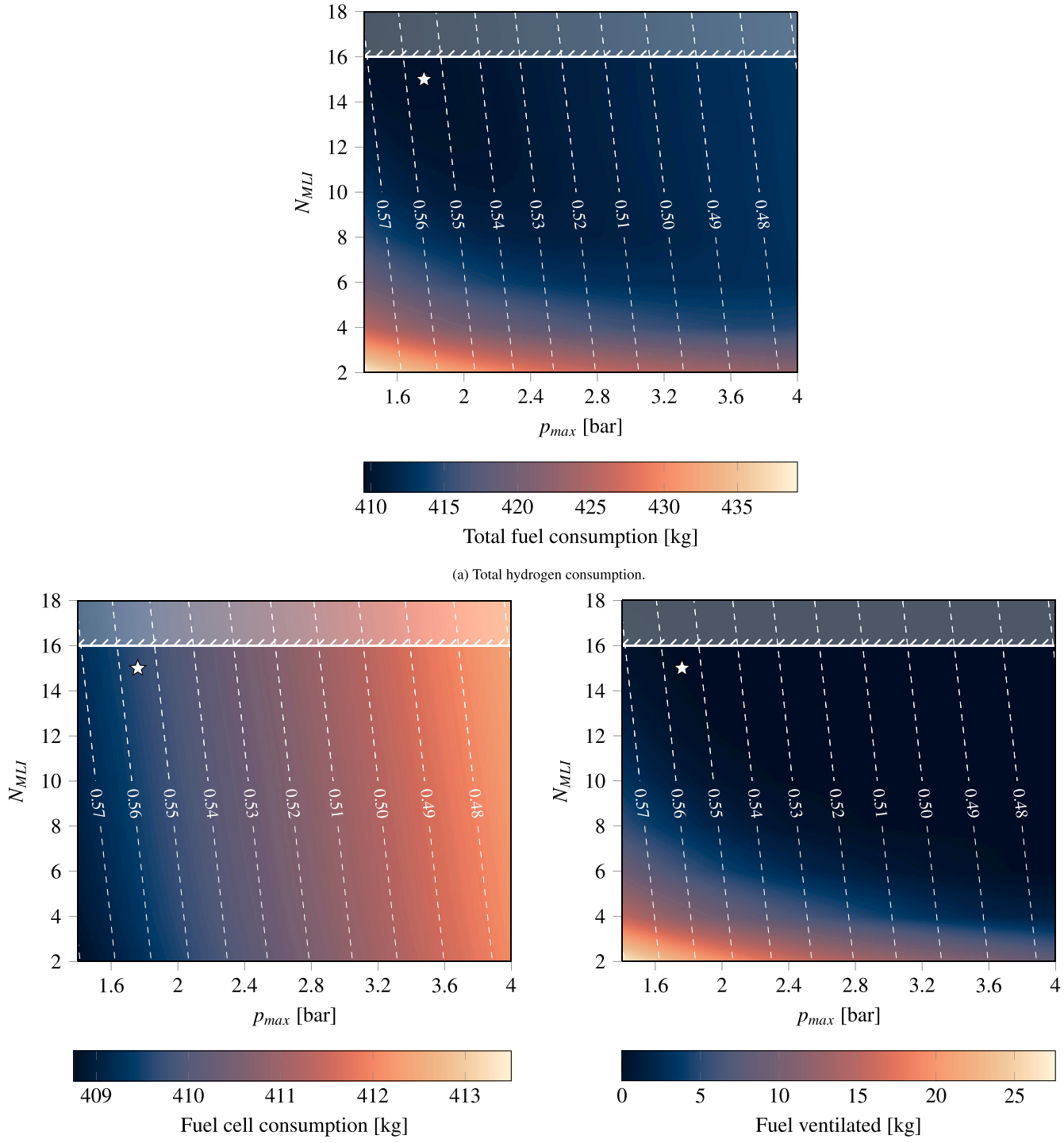

(a) Total hydrogen consumption.

(b) Hydrogen consumed by the fuel cell stacks.

(c) Hydrogen ventilated.

Fig. 7. Hydrogen consumption for parametric mission analysis of tank design. Tank gravimetric index is indicated by the dashed contours.

boil-off never reaches the ventilation pressure. As will be more clearly seen in the next section, the slope of the range curve is dominantly a function of the amount of insulation being used.

5.5. Return-without-refuel range

To investigate the feasibility of operations in a region with LH_2 refueling only available at larger airports, a mission was set up to simulate a return-without-refuel trip. It should immediately be stressed that the rate by which the pressure increases in a tank is quite dependent on the fill level. Thus the on-ground ventilation rate due to boil-off must be solved for using the tank state as it arrives at the airport B on its first flight going from A–B. In addition, as the tank state when starting the return mission from B-A will be quite different, boil of rates are now also much higher. To analyze the return-without-refuel for the proposed aircraft, mission analysis is thus needed.

The optimal design from the previous tank parameter study along with three other design points were simulated for ground hold times between zero and 12 h at the destination airport. As seen in Fig. 9, the optimal design (p_{max} = 1.76 bar, N_{MLI} = 15) manages to retain 43.5%

Table 5
Specifications of the cryogenic tank system for optimal condition.

Parameter	Specification
Shape	Spherical
Fuel volume	3.5 m^3
Gas ullage	3%
Fill pressure	1.2 bar
Ventilation pressure	1.76 bar
Wall material	Aluminum 5083
Insulation type	Multi-layer insulation
Outer wall thickness	4.2 mm
Insulation thickness	7.5 mm (15 layers)
Inner wall thickness	2.0 mm
Outer diameter	1.91 m
Total tank mass	191.1 kg
Outer wall mass	127.1 kg
Insulation mass	4.6 kg
Inner wall mass	59.4 kg
Gravimetric index	0.555

Table 6
Summary of tank performance in the return-without-refuel mission.

	Design range retained	Time until ventilation	Range loss rate
p_{max} = 1.76 bar, N_{MLI} = 15	43.5%	1 h	3.7 NM/h
p_{max} = 1.76 bar, N_{MLI} = 6	41.9%	0 h	8.6 NM/h
p_{max} = 4.00 bar, N_{MLI} = 15	42.9%	6 h	3.8 NM/h
p_{max} = 4.00 bar, N_{MLI} = 6	42.8%	3 h	8.3 NM/h

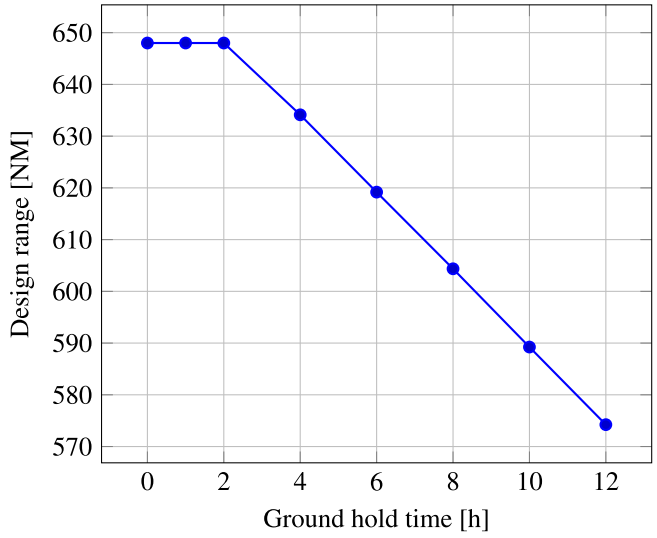

Fig. 8. Effect of ground hold time on range using optimal tank design parameters p_{max} = 1.76 bar, N_{MLI} = 15.

of the design range for a zero hours of ground hold. As argued earlier the resulting return-without-refuel range is not half of the design range, which is due to different fuel reserve requirements as well as the boil-off behavior changing with less fuel in the tank when flying back. Up to the one hour mark the return range is practically not affected by the boil-off, and it is only after this hold time that the range will start to decrease in a linear manner.

Since the p_{max} = 1.76 bar, N_{MLI} = 15 tank was optimized for the design mission it is interesting to study how tank parameter variation influences the return-without-refuel range. This is done by exploring three additional tanks, one with an increased ventilation pressure (p_{max} = 4.00 bar, N_{MLI} = 15), another with a reduced insulation (p_{max} = 1.76 bar, N_{MLI} = 6) and a final tank with both reduced insulation and increased ventilation pressure (p_{max} = 4.00 bar, N_{MLI} = 6).

First, the tank with an increased ventilation pressure is studied. The range becomes slightly lower for the zero ground hold time, due to being heavier and therefore burning off more fuel in the A–B part of the flight. On the other hand it is then able to stand on the ground up to six hours without having to ventilate fuel before then flying back. This effectively increases return-without-refuel range for ground hold times in excess of two hours, compared to the optimal tank. After about six hours this tank then starts to linearly decreasing in range as well, at the same rate as the optimal tank. This is since they are using the same insulation layer count and hence have very similar heat transfer rates.

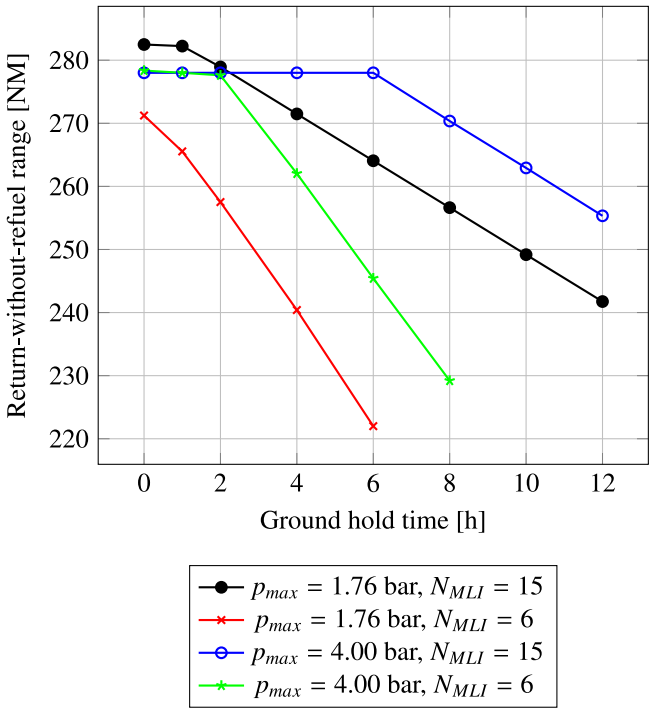

Fig. 9. Effect of ground hold time on return-without-refuel range for four tank designs.

The range for the tank with a high ventilation pressure, but a lower insulation layer count (p_{max} = 4.00 bar, N_{MLI} = 6) is able to match the performance of the previously mentioned tanks up to the two hour mark. Thereafter it starts to lose a significant amount of fuel on the ground due to its low amount of insulation.

The tank with the same ventilation pressure as the design mission-optimal tank, but with six MLI layers (p_{max} = 1.76 bar, N_{MLI} = 6), is shown to suffer a notable reduction in range. The range for zero ground hold time is more than 10 NM less than the design mission-optimal tank, which indicates that ventilation of fuel has occurred en-route to the destination airport. Thereafter the loss in range is very high due to the poorer insulation. Ventilation is needed almost immediately and already after six hours the range is estimated at 220 NM.

It is evident from this study that if the return-without-refuel capability is important to the airline operating the aircraft, this aspect must be considered carefully while choosing the design parameters. For example, if turnaround times at the destination airport is expected to be within the hour, then the design mission-optimal tank (p_{max} = 1.76 bar, N_{MLI} = 15) might be the best choice. For ground hold times longer than this however, it is clearly seen from Fig. 9 that the heaviest tank (p_{max} = 4.00 bar, N_{MLI} = 15) will be the best choice. Note that this tank is only slightly worse in total fuel consumption when flying the design mission (Fig. 7(a)) compared to the optimum.

The performance of the tanks is summarized in Table 6.

6. Conclusions

A short-range 50 PAX hydrogen fuel cell electric aircraft tailored for the Nordic market has been sized and its dynamic tank mission

performance analyzed. A conservative design approach of modifying an existing turboprop design was chosen, as to make entry-into-service feasible in the near future. The design range of the aircraft was decided using an air travel demand model over the Nordic countries, where the demand is projected to the year 2045. The chosen design range of 648 NM (1200 km) is able to cover the entirety of the flight distances in Sweden and Finland produced from the demand model, and a significant portion of the Norwegian demand.

When deciding the tank's ventilation pressure and insulation thickness, it was demonstrated that the tanks gravimetric index has little effect on this type of aircraft's total hydrogen consumption. The amount of fuel ventilated was shown to provide a much larger mission variation. The ventilated mass was both influenced by the ventilation pressure and the number of insulation layers, with the latter having the largest effect. The optimal tank for flying the design mission was found to have a ventilation pressure of 1.76 bar and 15 MLI layers.

Being able to fly return-without-refuel missions with this type of aircraft could potentially have a large impact on the pace by which hydrogen aircraft are introduced. The optimal tank for the design mission along with three other tanks were simulated. The design mission-optimal tank retained 43.5% of the design range up to one hour of ground hold, and after this it loses about 3.7 NM per hour of ground hold. A better design for this type of operation was a tank with higher ventilation pressure using the same insulation thickness (4 bar, 15 MLI layers). Although this tank has almost 10% lower gravimetric index compared to the design mission-optimal tank, it manages to retain 42.9% of the design range up to six hours on the ground compared to the optimal tank that only maintains 40.5%.

In conclusion, while designing tanks for a future airline it is key to consider not only the range but also the commercial value of being able to operate the aircraft at airports that do not have the hydrogen infrastructure available. The use of tank-heating may allow very high insulation to be used without reaching the limit of minimum tank pressure during climb. It should then be possible to get even closer to the 50% of the design range that may be achieved for return-without-refuel missions.

Declaration of competing interest

The authors declare that they have no known competing financial interests or personal relationships that could have appeared to influence the work reported in this paper.

Acknowledgments

The Competence Centre TechForH2 is hosted by Chalmers University of Technology and is financially supported by the Swedish Energy Agency (P2021-90268) and the member companies Volvo, Scania, Siemens Energy, GKN Aerospace, PowerCell, Oxeon, RISE, Stena Rederier AB, Johnsson Matthey and Insplorion.

Appendix A. Tank modeling

A.1. Mechanical design

The cryogenic pressure vessel is a near-vacuum double-wall design with the Multi-layer insulation (MLI) contained between the two walls. The tank is therefore subjected to both internal and external pressure loading. Fig. A.1 illustrates the construction of the tank.

At the maximum allowed pressure, the inner wall experiences a pressure difference of

$$\Delta p_{inner} = p_{max} - p_{MLI} \tag{A.1}$$

where p_{max} is the pressure at which gas ventilation is triggered and p_{MLI} is the vacuum jacket pressure. To account for manufacturing tolerances on the over-pressure ventilation system, [36] defines a design pressure which includes a 10% safety margin on top of p_{max}. Finally, extra safety margin is added to account for dynamic loading while flying. This is the "burst" pressure, which sets the inner wall thickness.

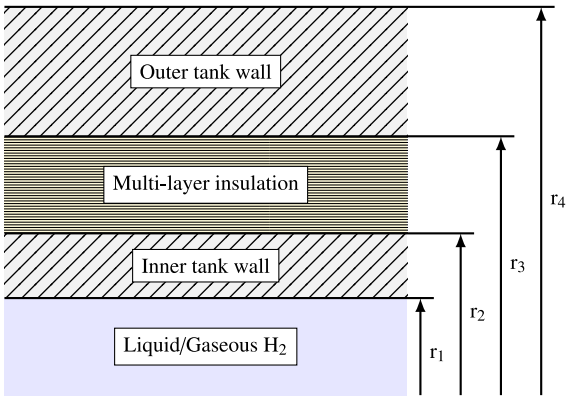

Fig. A.1. Tank cross-section.

Table A.1
Material properties and structural parameters used in the tank sizing.

Parameter	Value	Description
σ_y	228 MPa	Yield strength (AL5083) [65]
E	71 GPa	Young's modulus (AL5083) [65]
e_w	0.8	Weld weakness factor
K	0.5	Sphericity of end caps
SF_{inner}	2	Safety factor on yield strength
SF_{outer}	5	Safety factor on critical buckling pressure

$$p_{burst} = 2 \cdot p_{design,inner} = 2 \cdot (1.1 \Delta p_{inner}) \tag{A.2}$$

The inner wall thickness is then calculated according to [62] which accounts for the strength of the welds.

$$r_2 - r_1 = \begin{cases} \frac{2 \cdot p_{burst} \cdot r_2 \cdot K}{2 \cdot (\sigma_y / SF_{inner}) \cdot e_w - 2 \cdot p_{burst} \cdot (K - 0.1)} & \text{(spherical)} \\ \frac{2 \cdot p_{burst} \cdot r_2}{2 \cdot (\sigma_y / SF_{inner}) \cdot e_w - 0.8 \cdot p_{burst}} & \text{(cylindrical)} \end{cases} \tag{A.3}$$

The outer wall experiences external pressure loading and is therefore sensitive to buckling. The pressure difference is

$$\Delta p_{outer} = p_{\infty,max} - p_{MLI} \tag{A.4}$$

where $p_{\infty,max}$ is the worst case external pressure, taken at ISA sea-level conditions. We can then set a design pressure and a safety factor on the critical buckling pressure. A rather large safety factor is chosen as a compromised outer wall would cause failure of the MLI and subsequently catastrophic boil-off rates. A safety factor of five is therefore chosen. The required wall-thickness to prevent buckling is then found using formulas for critical buckling pressure on thin spherical and cylindrical shells [63].

$$r_4 - r_3 = \begin{cases} \sqrt{\frac{p_{design,outer} \cdot SF_{outer} \cdot r_4^2}{0.365 E}} & \text{(spherical)} \\ \left[\frac{\left(p_{design,outer} \cdot SF_{outer} \cdot L_{cyl} \cdot r_4^3 / (0.807 E) \right)^4}{(1/(1-\nu^2))^3} \right]^{1/10} & \text{(cylindrical)} \end{cases} \tag{A.5}$$

The mass of the MLI depends on the chosen layer density, total thickness and materials. As reported bulk densities from experiments are specific to the properties of a particular MLI system. Therefore, an approach of instead defining a layer specific area density (kg m^{-2}/layer) from experimental data ("45 layer standard MLI" [64]) was adopted.

Material and mechanical parameters for the tank walls are found in Table A.1.

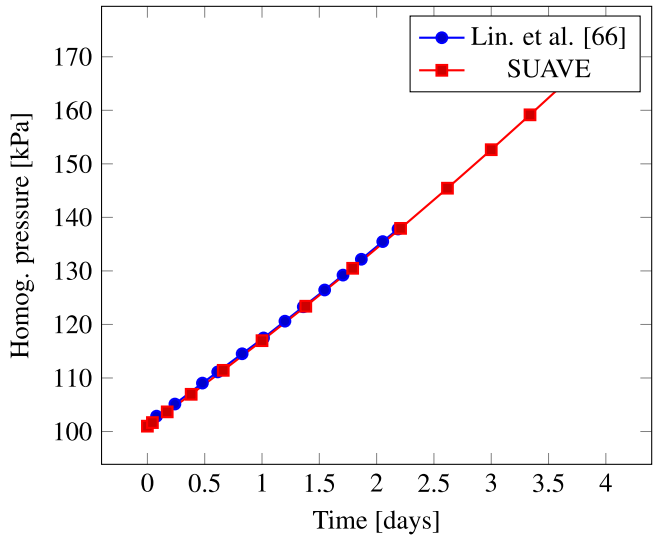

Fig. A.2. Pressure rise in a 52 m^3 tank with a 95% fill level at 100 W constant heat load [66].

A.2. Thermodynamic model

The method implemented to compute the tank pressure time variation throughout the mission is based on the work of [66]. The change in pressure is modeled by applying mass and energy conservation on a control volume. Mass transfer occurs through liquid fuel withdrawal to power the fuel cell and by ventilation of gaseous hydrogen. The ventilation is done to maintain the pressure below the ventilation pressure p_{max}.

Energy will be transferred to the control volume via heat transfer through the tank wall from the surrounding. The heat transfer rate is set to twice the theoretically computed rate following the suggestions of Lin et al. [66]. This is to safeguard towards additional heat transfer mechanisms such as liquid stratification, which is not modeled. Finally, a 30% increase of the heat transfer rate is applied in accordance with [36] to account for heat conduction through tank components such as its mounting structure and fuel lines. The equation for the time pressure derivative is then:

$$\frac{dp}{dt} = 2\frac{\Phi}{V}\left[1.3Q - \Delta h\left(\dot{m}_{gas} + \rho^*\left(\dot{m}_{gas} + \dot{m}_{liquid}\right)\right)\right] \tag{A.6}$$

where

$$p^* = \frac{\rho_{gas}}{\rho_{gas} + \rho_{liquid}} \tag{A.7}$$

and the energy derivative is defined as

$$\Phi = \frac{1}{\rho\frac{\partial u}{\partial p}} \tag{A.8}$$

The state functions for the liquid and gas are calculated as a function of the homogeneous pressure using the thermodynamic library CoolProp [67]. The internal energy derivative in the energy derivative equation is approximated using finite differencing.

The numerical accuracy of SUAVE's method of spectral integration matrices is verified by replicating a simulation of a 52 m^3 tank with a 5% gas ullage, which is subjected to a constant heat load of 100 W at a fill level of 95%. As seen in Fig. A.2, SUAVE is able to capture the behavior predicted by [66] with good accuracy, even with as few as 16 cosinus-spaced spectral collocation points. Note that the 30% increased heat transfer included in Eq. (A.6) is not considered here, to be consistent with the modeling proposed in [66].

In order to model the pressure changes in the tank due to varying flight conditions, a heat transfer model is needed. The mechanisms for heat transfer in the system are:

Table A.2
Model fitting parameters for the MLI system.

Parameter	Value
C_1	$4.43 \cdot 10^{-11}$
C_2	3.91
C_3	$8.03 \cdot 10^{-10}$
C_g	$1.46 \cdot 10^{4}$
n_g	0.53

1. External convection and radiation
2. Conduction through the tank walls and insulation
3. Internal convection

Free convection on the tank's external and internal surfaces is approximated using Nusselt-number correlations for a vertical flat plate with a length equal to the tank diameter [68]:

$$\overline{Nu} = \left[0.825 + \frac{0.387Ra^{1/6}}{(1 + (0.492/Pr)^{9/16})^{8/27}}\right]^2 \tag{A.9}$$

In the case of the external free convection, the temperature and pressure are set to ISA conditions for the current altitude in a given mission segment time step. On the inside of the tank, the free convection is calculated separately for the gas and liquid phase. Radiative heat transfer occurs on the external tank wall surface which is modeled as a gray body. The emissivity is set to 0.1. The external and internal tank walls are assumed to have zero thermal resistance due to their high conductivity, and instead only the MLI provides thermal resistance. The heat flux through the MLI layers is evaluated in bulk (instead of a discretized "layer-by-layer" method) using an adaptation [69] of the semi-empirical Lockheed model [70]:

$$\begin{aligned} q_{MLI} = {} & C_1 N_t^{C_2}\frac{(T_H + T_C)(T_H - T_C)}{2(N_{MLI} + 1)} \\ & + C_3\epsilon\frac{T_H^{4.67} - T_C^{4.67}}{N_{MLI}} + C_g\frac{p_{MLI}}{N_{MLI}}(T_H^{n_g} - T_C^{n_g}) \end{aligned} \tag{A.10}$$

where N_{MLI} is the number of radiation shield layers and N_t the layer density. T_C and T_H are the temperatures on the cold and hot boundaries. C_1, C_2 and C_3 are model parameters for the radiation shields, and C_g and n_g are parameters for the gas in the near-vacuum, in this case nitrogen gas. Model parameters used for the MLI are for double alumnized mylar radiation shields with Tissuglas spacer material ("DAM/Tissuglas") as it showed low degradation in thermal performance when subjected to various amounts of compression [69]. Table A.2 lists the parameter values for the chosen MLI system. Chosen vacuum level was $p_{MLI} = 1$ mBar, and the layer density $N_t = 50$ layers/inch.

The heat transfer in the system can then be represented by

$$\begin{aligned} Q_{conv,air} + Q_{rad} &= Q_{MLI} \\ Q_{conv,gas} + Q_{conv,liq} &= Q_{MLI} \end{aligned} \tag{A.11}$$

which forms a system of non-linear equations where the surface temperature of the tank's outer and inner surface are unknown. These two unknowns are then solved for numerically.

Appendix B. Fuel cell modeling

B.1. Electrochemical model

The hydrogen fuel flow requirement is derived from a fuel cell voltage model [54]. The model accounts for activation losses due to reaction kinetics, ohmic losses due to electrical resistance and concentration losses due to mass transport. The output voltage of a single fuel

Table B.1
Model parameters obtained from [55] assuming a fuel cell pressure of 2.5 bar.

Parameter	Value
E_r	1.1782 V
i_{0C}	0.0001
α_C	0.22
i_{0A}	0.1
α_A	0.5
ASR_Ω	0.04 Ω cm^2
i_L	2.45 A/cm^2
i_{leak}	0.30 A/cm^2
C	0.035 V

cell is modeled from:

$$\begin{aligned} v &= E_r - \eta_{act} - \eta_{ohm} - \eta_{conc} \\ \eta_{act} &= \left[a_A + b_A \log\left(i + i_{leak}\right)\right] + \left[a_C + b_C \log\left(i + i_{leak}\right)\right] \\ \eta_{ohm} &= i ASR_\Omega \\ \eta_{conc} &= C \log \frac{i_L}{i_L - \left(i + i_{leak}\right)} \end{aligned} \tag{B.1}$$

where i is the current density. The activation loss constants for the anode and cathode are defined by:

$$\begin{aligned} a_A &= -\frac{RT}{\alpha_A n_A F} \log i_{0A} \\ b_A &= \frac{RT}{\alpha_A n_A F} \\ a_C &= -\frac{RT}{\alpha_C n_C F} \log i_{0C} \\ a_C &= \frac{RT}{\alpha_C n_C F} \end{aligned} \tag{B.2}$$

where T is the working temperature (80 °C), R is the universal gas constant and F is the Faraday's constant. n_A and n_C are the electrons captured at the anode and cathode, respectively.

The true efficiency, a measurement of how much chemically stored energy is converted into electrical energy, is defined as

$$\eta = \frac{v}{E_h} \tag{B.3}$$

where E_h is the voltage potential corresponding to the higher heating value of hydrogen.

Although the equations presented above represent a generic framework to predict the single cell output voltage, a number of parameters still have to be specified to make the model practically useful. Herein, these parameters are derived from the work of Datta et al. [55] for a fuel cell operating pressure of 2.5 bar. The resulting parameters are collected in Table B.1. The functional relationship between current density and cell voltage, defined by Eqs. (B.1), (B.2) and the parameters collected in Table B.1, is usually referred to as the single cell polarization curve.

B.2. Stack design

Once the fuel cell chemistry, stack operating pressure and design point on the polarization curve are set, the main remaining parameters needed are the output power and voltage. Maximum cell efficiency is used to select the design point on the polarization curve. The required design stack power, P_D, will set the total fuel cell area of the stack. It should be noted that the required design power for the stack also has to cover the BoP. Because the fuel cells are connected in series, the number of cells will be determined by the stack voltage V_D. With the design point, number of cells and cell area set, it is now possible to calculate the resulting power, current, voltage and efficiency at any input current density i [55]. Data for the resulting stack design are presented in Table 4 in the main paper text.

B.3. Balance of plant components

Apart from the main power requirement arising from driving the propellers a number of smaller auxiliary components need power as well. The total power requirement P is obtained from:

$$P = P_{prop} + P_{air} + P_{cool} \tag{B.4}$$

where P_{air} is the power needed for driving the air compressor and P_{cool} is the power required by the coolant pumps. Eq. (B.4) is referred to as the balance of plant (BoP) equation and the air compressor and the coolant pumps are referred to as balance of plant components. Compression of the air is needed on the ground when running the stack at elevated operating pressures, and at altitude regardless of stack pressure. The compressor is sized for the most unfavorable operating point, which is at cruise altitude, where the conditions are

$$\begin{aligned} p_1 &= p_{cruise,ISA} + q_{cruise,ISA} \\ T_1 &= T_{cruise,ISA} \end{aligned} \tag{B.5}$$

where $p_{cruise,ISA}$ is the static pressure at cruise altitude (ISA conditions assumed), $q_{cruise,ISA}$ the dynamic pressure at cruise and $T_{cruise,ISA}$ the static temperature. This expression assumes full pressure recovery in the inlet. A utilization factor of two was used for the air system (twice the amount of air needed for the reaction is ingested).

A small amount of energy can be recovered in the stack air outlet through a turbine which is assumed to expand to ambient pressure.

$$P_{air} = P_{comp} - P_{turb} \tag{B.6}$$

The cooling system must be capable of rejecting the heat produced by the fuel cells at any given point during the mission. The system is sized to the worst-case operating point, which is assumed to be during $P = P_D$ at sea-level conditions with an ambient temperature $T_1 = 40$ °C

$$Q_{stack} = P\left(\frac{1}{\eta_D} - 1\right) \tag{B.7}$$

where

$$\eta_D = \eta \frac{P_{prop}}{P} \tag{B.8}$$

is the system efficiency.

Heat is partially rejected through the stack's air system. As a compressor is used in the air inlet, it is assumed only the exhaust is able to reject heat. The remaining heat is rejected by the liquid cooling system, which consists of coolant lines, a pump and radiators. The BoP (Eq. (B.4)) has one unknown, the total stack power P, and is solved for during the sizing routine as well as throughout the mission. Finally, with the stack power known, the fuel consumption can be calculated. The hydrogen mass flow to the fuel cell stack will then be

$$\dot{m}_{liquid} = f_H S_H \frac{m_H}{NF} \frac{P}{v} \tag{B.9}$$

where $f_H = 1$ is the hydrogen utilization factor (all incoming hydrogen is reacted), $S_H = 1$ is the moles of hydrogen to produce $N = 2$ moles of electrons, $m_H = 2.01588 \cdot 10^{-3}$ kg/mole the molecular weight of hydrogen.

References

[1] Färdplan för fossilfri konkurrenskraft, flygbranschen. Tech. rep, Svenskt Flyg; 2018.
[2] Graver B, Dan R, Sola Z. CO_2 emissions from commercial aviation: 2013, 2018, and 2019. Tech. rep, ICCT; 2020.
[3] Technology evaluator first global assessment 2020. Technical report, Clean Sky 2 project; 2021, URL https://cleansky.paddlecms.net/sites/default/files/2021-10/TE-FGA-TR_en.pdf.
[4] Heart Aerospace. ES-30. 2023, URL https://heartaerospace.com/es-30/. [Accessed 2023-11-14].
[5] Zero Avia. ZA600. 2023, URL https://zeroavia.com/za600/. [Accessed 2023-11-14].

[6] Zero Avia. ZA2000. 2023, URL https://zeroavia.com/za2000/. [Accessed 2023-11-14].

[7] AIRBUS. ZEROe. 2023, URL https://www.airbus.com/en/innovation/low-carbon-aviation/hydrogen/zeroe/. [Accessed 2023-11-14].

[8] Mukhopadhaya J, Rutherford D. Performance analysis of evolutionary hydrogen-powered aircraft. Tech. rep., ICCT; 2022, URL www.theicct.org.

[9] Hydrogen-powered aviation – A fact-based study of hydrogen technology, economics, and climate impact by 2050. Technical report, Clean Sky 2 project; 2020, http://dx.doi.org/10.2843/471510, URL https://data.europa.eu/doi/10.2843/471510.

[10] Gierens K. Theory of contrail formation for fuel cells. Aerospace 2021;8. http://dx.doi.org/10.3390/aerospace8060164.

[11] Schumann U. On conditions for contrail formation from aircraft exhausts. Meteorol Z 1996;5:4–23.

[12] Royal NLR– Netherlands Aerospace Centre. Technological developments and radical innovations. 2023, URL https://www.nlr.org/focus-area/programmes/programme-climate-neutral-aviation/technological-developments-and-radical-innovations/.

[13] Rompokos P, Rolt A, Nalianda D, Isikveren AT, Senné C, Grönstedt T, Abedi H. Synergistic technology combinations for future commercial aircraft using liquid hydrogen. J Eng Gas Turbines Power 2021;143. http://dx.doi.org/10.1115/1.4049694.

[14] Sefain MJ. Hydrogen Aircraft Concepts & ground support (Ph.D. thesis), Cranfield University; 2005.

[15] Boll M, Corduan M, Biser S, Filipenko M, Pham QH, Schlachter S, Rostek P, Noe M. A holistic system approach for short range passenger aircraft with cryogenic propulsion system. Supercond Sci Technol 2020;33. http://dx.doi.org/10.1088/1361-6668/ab7779.

[16] Xisto C, Lundbladh A. Design and performance of liquid hydrogen fueled aircraft for year 2050. In: International council of the aeronautical sciences. 2022.

[17] Prewitz M, Schwärzer J, Bardenhagen A. Potential analysis of hydrogen storage systems in aircraft design. Int J Hydrogen Energy 2023.

[18] Jagtap SS, Childs PR, Stettler ME. Performance sensitivity of subsonic liquid hydrogen long-range tube-wing aircraft to technology developments. Int J Hydrogen Energy 2023.

[19] Verstraete D. On the energy efficiency of hydrogen-fuelled transport aircraft. Int J Hydrogen Energy 2015;40:7388–94. http://dx.doi.org/10.1016/j.ijhydene.2015.04.055.

[20] Guynn MD, Freeh JE, Olson ED. Evaluation of a hydrogen fuel cell powered blended-wing-body aircraft concept for reduced noise and emissions. Technical Memorandum NASA/TM-2004-212989, NASA; 2004.

[21] Burschyk T, Cabac Y, Silberhorn D, Boden B, Nagel B. Liquid hydrogen storage design trades for a short-range aircraft concept. CEAS Aeronaut J 2023;1–15.

[22] Zaghari B, Zhou T, Enalou HB, Pontika E, Laskaridis P. The impact of multi-stack fuel cell configurations on electrical architecture for a Zero Emission Regional aircraft. AIAA SCITECh 2023 forum, 2023, p. 1593.

[23] Gao Y, Jausseme C, Huang Z, Yang T. Hydrogen-powered aircraft: Hydrogen–electric hybrid propulsion for aviation. IEEE Electrif Mag 2022;10(2):17–26. http://dx.doi.org/10.1109/MELE.2022.3165725.

[24] Verstraete D, Hendrick P, Pilidis P, Ramsden K. Hydrogen fuel tanks for subsonic transport aircraft. Int J Hydrogen Energy 2010;35(20):11085–98. http://dx.doi.org/10.1016/j.ijhydene.2010.06.060, URL https://www.sciencedirect.com/science/article/pii/S036031991001236X. Hyceltec 2009 Conference.

[25] Mukhopadhaya J. Performance analysis of fuel cell retrofit aircraft. Tech. rep., ICCT; 2023.

[26] Seeckt K, Heinze W, Scholz D. Hydrogen powered freighter aircraft - the final results of the green freighter project. In: International council of the aeronautical sciences. 2010, URL https://www.icas.org/ICAS_ARCHIVE/ICAS2010/PAPERS/228.PDF.

[27] Rosli R, Sulong A, Daud W, Zulkifley M, Husaini T, Rosli M, Majlan E, Haque M. A review of high-temperature proton exchange membrane fuel cell (HT-PEMFC) system. Int J Hydrogen Energy 2017;42(14):9293–314. http://dx.doi.org/10.1016/j.ijhydene.2016.06.211, URL https://www.sciencedirect.com/science/article/pii/S0360319915313069. Special Issue on Sustainable Fuel Cell and Hydrogen Technologies: The 5th International Conference on Fuel Cell and Hydrogen Technology (ICFCHT 2015), 1-3 September 2015, Kuala Lumpur, Malaysia.

[28] Palladino V, Jordan A, Bartoli N, Schmollgruber P, Pommier-Budinger V, Benard E. Preliminary studies of a regional aircraft with hydrogen-based hybrid propulsion. AIAA aviation forum, 2021, http://dx.doi.org/10.2514/6.2021-2411.

[29] Rischmüller UCJ, Lessis A, Egerer P, Hornung M. Conceptual design of a hydrogen-hybrid dual-fuel regional aircraft retrofit. Aerospace 2024;11(2). http://dx.doi.org/10.3390/aerospace11020123, URL https://www.mdpi.com/2226-4310/11/2/123.

[30] Tove Lundberg N. All airports in the nordic region by a degree of urbanisation. 2023, URL https://nordregio.org/maps/all-airports-in-the-nordic-region-by-a-degree-of-urbanisation/. [Accessed 2023-09-13].

[31] Amadori K, Jouannet C, Zhao X. Towards zero-emission transportation in Scandinavia. In: AIAA SCITECh 2023 forum. http://dx.doi.org/10.2514/6.2023-1909, URL https://arc.aiaa.org/doi/abs/10.2514/6.2023-1909.

[32] Swedavia. Destinationsstatistik 2019. Swedavia; 2019, URL https://www.swedavia.se/globalassets/statistik/destinationsstatistik_2019.xlsx. [Accessed 2023-04-06].

[33] Brewer GD, Morris RE, Lange RH, Moore JW. Study of the application of hydrogen fuel to long-range subsonic transport aircraft. Contractor Report NASA/CR-1975-132558, Burbank: NASA; 1975.

[34] Brewer GD, Morris RE. Study of LH2-fueled subsonic passenger transport aircraft. Contractor Report NASA/CR-1976-144935, Burbank: NASA; 1976.

[35] Gomez A, Smith H. Liquid hydrogen fuel tanks for commercial aviation: Structural sizing and stress analysis. Aerosp Sci Technol 2019;95:105438. http://dx.doi.org/10.1016/j.ast.2019.105438, URL https://www.sciencedirect.com/science/article/pii/S1270963818304139.

[36] Brewer GD. Hydrogen aircraft technology. CRC Press; 1991.

[37] Schmidtchen U, Behrend E, Pohl HW, Rostek N. Hydrogen aircraft and airport safety. Renew Sustain Energy Rev 1997;1(4):239–69. http://dx.doi.org/10.1016/S1364-0321(97)00007-5, URL https://www.sciencedirect.com/science/article/pii/S1364032197000075.

[38] Faaß R. CRYOPLANE flugzeuge mit Wasserstoffantrieb. 2001, URL https://www.fzt.haw-hamburg.de/pers/Scholz/dglr/hh/text_2001_12_06_Cryoplane.pdf. Presentation.

[39] Liquid hydrogen fuelled aircraft – system analysis. Final technical report, Cryoplane project; 2003, URL https://www.fzt.haw-hamburg.de/pers/Scholz/dglr/hh/text_2004_02_26_Cryoplane.pdf.

[40] Boeing. Phantom eye. 2022, URL https://www.boeing.com/defense/phantom-eye/. [Accessed 2022-10-06].

[41] Boeing. Boeing phantom eye completes 1st autonomous flight. 2012, URL https://boeing.mediaroom.com/2012-06-04-Boeing-Phantom-Eye-Completes-1st-Autonomous-Flight. [Accessed 2022-10-06].

[42] Universal Hydrogen. Universal hydrogen successfully completes first flight of hydrogen regional airliner. 2023, URL https://hydrogen.aero/press-releases/universal-hydrogen-successfully-completes-first-flight-of-hydrogen-regional-airliner/.

[43] Sorensen B, Spazzafumo G. Hydrogen and fuel cells: emerging technologies and applications. Academic Press; 2018.

[44] Contreras A, Yiğit S, Özay K, Veziroğlu T. Hydrogen as aviation fuel: A comparison with hydrocarbon fuels. Int J Hydrogen Energy 1997;22(10):1053–60. http://dx.doi.org/10.1016/S0360-3199(97)00008-6, URL https://www.sciencedirect.com/science/article/pii/S0360319997000086.

[45] Yanxing Z, Maoqiong G, Yuan Z, Xueqiang D, Jun S. Thermodynamics analysis of hydrogen storage based on compressed gaseous hydrogen, liquid hydrogen and cryo-compressed hydrogen. Int J Hydrogen Energy 2019;44:16833–40. http://dx.doi.org/10.1016/j.ijhydene.2019.04.207.

[46] Zhang M, Lv H, Kang H, Zhou W, Zhang C. A literature review of failure prediction and analysis methods for composite high-pressure hydrogen storage tanks. Int J Hydrogen Energy 2019;44(47):25777–99.

[47] Arnold SM, Sullivan RM, Manderscheid JM, Murthy PLN. Review of current state of the art and key design issues with potential solutions for liquid hydrogen cryogenic storage tank structures for aircraft applications. Technical Memorandum NASA/TM-2006-214346, National Aeronautics and Space Administration; 2006.

[48] Sippel M, Kopp A, Mattsson D, Freund J, Koussios S. Final results of advanced cryo-tanks research project CHATT. 2015.

[49] Huete J, Pilidis P. Parametric study on tank integration for hydrogen civil aviation propulsion. Int J Hydrogen Energy 2021;46:37049–62. http://dx.doi.org/10.1016/j.ijhydene.2021.08.194.

[50] Zheng J, Chen L, Wang J, Xi X, Zhu H, Zhou Y, Wang J. Thermodynamic analysis and comparison of four insulation schemes for liquid hydrogen storage tank. Energy Convers Manage 2019;186:526–34. http://dx.doi.org/10.1016/j.enconman.2019.02.073, URL https://www.sciencedirect.com/science/article/pii/S019689041930264X.

[51] Jiang W, Sun P, Li P, Zuo Z, Huang Y. Transient thermal behavior of multi-layer insulation coupled with vapor cooled shield used for liquid hydrogen storage tank. Energy 2021;231:120859. http://dx.doi.org/10.1016/j.energy.2021.120859, URL https://www.sciencedirect.com/science/article/pii/S0360544221011075.

[52] Lukaczyk T, Wendorff AD, Botero E, Macdonald T, Momose T, Variyar A, Vegh JM, Colonno M, Economon TD, Alonso JJ, Orra TH, Silva CID. SUAVE: An open-source environment for multi-fidelity conceptual vehicle design.

[53] Abuzant S, Jemei S, Hissel D, Boulon L, Agbossou K, Gustin F. A review of multi-stack PEM fuel cell systems: Advantages, challenges and on-going applications in the industrial market. In: 2017 IEEE vehicle power and propulsion conference. VPPC, IEEE; 2017, p. 1–6.

[54] O'Hayre R, Cha S-W, Colella W, Prinz FB. Fuel cell fundamentals, third ed.. Nashville, TN: John Wiley & Sons; 2016.

[55] Datta A. PEM fuel cell model for conceptual design of hydrogen eVTOL aircraft. NASA; 2021.

[56] SUAVE. SUAVE. 2023, URL https://suave.stanford.edu/.

[57] Wendorff A, Variyar A, Ilario C, Botero E, Capristan F, Smart J, Alonso J, Kulik L, Clarke M, Colonno M, Kruger M, Vegh JM, Goncalves P, Erhard R, Fenrich R, Orra T, St. Francis T, MacDonald T, Momose T, Economon T, Lukaczyk T, Maier W. SUAVE: An aerospace vehicle environment for designing future aircraft. 2020, URL https://github.com/suavecode/SUAVE.

[58] Allidieris L, Janin F. Tanks (including insulation). Task Technical Report 3.6.2.1, Cryoplane project; 2002.
[59] Adler EJ, Martins JR. Hydrogen-powered aircraft: Fundamental concepts, key technologies, and environmental impacts. Prog Aerosp Sci 2023;141:100922. http://dx.doi.org/10.1016/j.paerosci.2023.100922, URL https://www.sciencedirect.com/science/article/pii/S0376042123000386. Special Issue on Green Aviation.
[60] Padgett E, Kleen G. Automotive fuel cell targets and status, DOE hydrogen and fuel cells program record. Tech. Rep DOE Record #20005, US Department of Energy; 2020.
[61] El-Refaie A, Osama M. High specific power electrical machines: A system perspective. CES Trans Electr Mach Syst 2019;3:88–93. http://dx.doi.org/10.30941/CESTEMS.2019.00012.
[62] Barron RF. Cryogenic Systems. second ed.. Monographs on cryogenics, New York, NY: Oxford University Press; 1985.
[63] Young WC, Budynas RG, Sadegh A. Roark's Formulas for Stress and Strain. 8. New York, NY: McGraw-Hill Professional; 2011.
[64] Hastings LJ, Hedayat A, Brown T. Analytical modeling and test correlation of variable density multilayer insulation for cryogenic storage. Technical Memorandum NASA/TM-2004-213175, NASA; 2004.
[65] Aerospace Specification Metals. Aluminum 5083-H116; 5083-H321. 2023, URL https://asm.matweb.com/search/SpecificMaterial.asp?bassnum=ma5083h116. [Accessed 2023-11-19].
[66] Lin CS, Dresar NTV, Hasan MM. A pressure control analysis of cryogenic storage systems. Technical Memorandum NASA/TM-1991-194498, NASA; 1991.
[67] Bell IH, Wronski J, Quoilin S, Lemort V. Pure and pseudo-pure fluid thermophysical property evaluation and the open-source thermophysical property library CoolProp. Ind Eng Chem Res 2014;53(6):2498–508. http://dx.doi.org/10.1021/ie4033999, arXiv:http://pubs.acs.org/doi/pdf/10.1021/ie4033999.
[68] Incropera FP, Dewitt DP, Bergman TL, Lavine AS. Incropera's Principles of Heat and Mass Transfer. John Wiley & Sons; 2017.
[69] Verstraete D. The Potential of Liquid Hydrogen for Long Range Aircraft Propulsion (Ph.D. thesis), Cranfield University; 2009.
[70] Keller CW, Cunnington GR, Glassford AP. Thermal performance of multilayer insulations. Contractor Report NASA/CR-1974-134477, NASA; 1974.